This manuscript is a preprint and will be submitted to Earth and Planetary Science Letters. Subsequent versions of this manuscript may have slightly different content. If accepted, the final version of this manuscript will be available via the ‘Peer-reviewed Publication DOI’ link on the right-hand side of this webpage. Please feel free to contact any of the authors; we welcome feedback.

DID DEGLACIATION OF THE GREENLAND ICE SHEET CAUSE A LARGE EARTHQUAKE AND TSUNAMI AROUND 10,600 YEARS AGO?

R. Steffen[1*], H. Steffen[1], R. Weiss[2,3], B. S. Lecavalier[4], G. A. Milne[5], Sarah A. Woodroffe[6], O. Bennike[7]

1 - Lantmäteriet, Lantmäterigatan 2, 80182 Gävle, Sweden

2 - Department of Geosciences, Virginia Tech, 4044 Derring Hall, Blacksburg, VA 24061, U.S.A.

3 - Center for Coastal Studies, Virginia Tech, 926 West Campus Drive, Blacksburg, VA 24061, U.S.A.

4 - Department of Physics and Physical Oceanography, Memorial University of Newfoundland, St. John's, Newfoundland A1B 3X7, Canada

5 - Department of Earth Sciences, University of Ottawa, Marion Hall, 140 Louis Pasteur, Ottawa, Ontario K1N 6N5, Canada

6 - Department of Geography, Durham University, Lower Mountjoy, South Road, Durham, DH1 3LE, UK

7 - Geological Survey of Denmark and Greenland, Øster Voldgade 10, 1350 Copenhagen K, Denmark

*Corresponding author: rebekka.steffen@lm.se

HIGHLIGHTS

- First stress calculations for Greenland due to ice-sheet melting.
- Glacially-triggered earthquake occurred close to Nanortalik in the Holocene.
- Relative-sea level data affected by glacially-triggered earthquakes.
- Earthquake induced palaeotsunami in the North Atlantic.

ABSTRACT

Due to their large mass, ice sheets induce significant stresses in the Earth's crust. Stress release during deglaciation can trigger large-magnitude earthquakes, as indicated by surface faults in northern Europe. Although glacially-induced stresses have been analyzed in northern Europe, they have not yet been analyzed for Greenland. We know that the Greenland Ice Sheet experienced a large melting period in the early Holocene, and so here, we analyze glacially-induced stresses during deglaciation for Greenland for the first time. Instability occurs in southern Greenland, where we use a combined analysis of past sea level indicators and a model of glacially-triggered fault reactivation to show that deglaciation of the Greenland Ice Sheet may have caused a large magnitude earthquake around 10,600 years ago offshore south-western Greenland. The earthquake may have shifted relative sea level observations by several meters. If the earthquake-induced stress release was created during a single event, it could have produced a tsunami in the North Atlantic Ocean with runup heights of up to 5 m in the British Isles and up to 7.5 m along Canadian coasts.

KEYWORDS

Glacial isostatic adjustment; Relative sea-level data; Tsunami; Greenland; Glacially-induced faulting

1. INTRODUCTION

The growth and decay of ice sheets during a glacial/interglacial cycle affect a multitude of processes on the surface as well as in the interior of the Earth, which are commonly termed glacial isostatic adjustment (GIA). For example, the mass redistribution of water between the ice sheets and the oceans causes changes in the Earth's shape, gravity, rotation and sea level (Wu & Peltier, 1982). This climate-driven surface loading results also in significant horizontal and vertical stress changes due to the enormous mass of the ice sheets (Johnston, 1987; Fig. 1A). In a compressional stress setting, where horizontal stresses are larger than the vertical stress, fault slip and thus earthquake activity is inhibited (Johnston, 1987), hence explaining the relatively low seismic activity in present-day Greenland (Voss et al., 2007). During deglaciation, however, the vertical stress decreases in relation to the vanishing ice, but the decrease of horizontal stresses is delayed due to bending of the lithosphere and the viscoelastic nature of the underlying mantle (Johnston, 1987; Wu & Hasegawa, 1996), promoting fault reactivation in a compressional stress setting (Fig. 1B). Deglacial reactivation of faults has occurred in northern Europe, where more than a dozen glacially-induced faults (GIFs) have been identified, showing offsets of up to 30 m at the surface (Lagerbäck & Sundh, 2008). They were reactivated by earthquakes with moment magnitudes of up to 8.2 (Arvidsson, 1996) during the deglaciation and shortly after to release the stresses induced by the glacial cycle. However, knowledge is limited for the currently glaciated regions of Greenland and Antarctica, even though Arvidsson (1996) pointed to the possibility that future deglaciation of the ice sheets may cause large earthquakes. Although the Greenland Ice Sheet has exhibited accelerating mass loss over the past few decades (McMillan et al., 2016), there is no evidence yet of a related increase in seismic activity (Voss et al., 2007; Olivieri & Spada, 2015).

Here we consider the deglaciation of the Greenland Ice Sheet since the Last Glacial Maximum around 20 ka before present (BP) to present, during which the ice sheet lost ~40%

of its mass (Lecavalier et al., 2014; Khan et al., 2016). We present the first calculations of stress changes induced by ice-mass loss in the early Holocene to assess whether and where glacially-triggered earthquakes were likely to have occurred. Our modeling results indicate that southern Greenland is the most prone to glacially-induced faulting. Using a faulting scenario that is consistent with the geological records, we show that a modelled fault could have been reactivated producing an earthquake and potentially a tsunami wave (Fig. 1C) during the early Holocene, and we compute the wave height distribution around North Atlantic coasts. As this analysis consists of a combination of several different methods, we introduce in the following sections the methods in logical order together with their corresponding results.

Figure 1

2. RESULTS AND DISCUSSION

A recent model reconstruction of the Greenland Ice Sheet (termed Huy3; Lecavalier et al., 2014) and its appendant (optimal) Earth viscosity model (lithospheric thickness of 120 km, upper mantle viscosity of $5 * 10^{20}$ Pa*s, lower mantle viscosity of $2 * 10^{21}$ Pa*s) and ocean-load model are used to calculate stress changes during the past 120,000 years for the whole of Greenland in a compressional stress setting. Our modelling procedure follows the approach described in Wu (2004) which uses a three-dimensional (3D) flat model using the finite-element software ABAQUS (Hibbitt et al., 2016) to estimate GIA-induced displacements and stresses. The model consists of eleven layers with different material parameters covering a depth range from the Earth’s surface to the core-mantle boundary. The upper four layers are purely elastic and form the lithosphere, while the lower seven layers represent the visco-elastic mantle. The horizontal length scale of the finite elements is 50 km and the vertical length scale gradually increases from 5 km in the crust (upper 30 km of the lithosphere) to a maximum of 590 km in the lower mantle. No lateral variations of the material parameters are used. Earth model variations have only a small effect on the reactivation time for faults located between the ice margin and the ice-sheet centre (e.g., Kaufmann et al., 2005; Steffen et al., 2014a; Brandes et al., 2019; Steffen et al., 2019), and the usage of a 3D Earth model is therefore not needed here. The model domain features Greenland in its centre and is square in shape with a side length of 4500 km. The model domain also includes parts of North America and northern Europe which are, as in Lecavalier et al. (2014), loaded with a North American ice sheet model by Tarasov et al. (2012) and a Fennoscandian and Iceland ice sheet model by Peltier (2004) to incorporate the GIA response from these regions as well. Ocean mass changes are not calculated within the GIA model directly as the here applied flat model approximation is not able to solve the sea-level equation. Thus, an ocean load obtained from a 1D spherical GIA calculation (Mitrovica et al., 1994) is used, which is based on the same ice and Earth model configuration as the finite-element model. The ice and ocean load are then applied together to the Earth model to obtain GIA-induced displacement and stresses. However, the usage of the finite-element methodology in ABAQUS requires the transformation of the obtained stress tensor to GIA stresses (Steffen et al., 2015) while the displacement vector is the same. The calculated GIA stresses are then combined with tectonic background stresses to analyse the potential for GIF reactivation (Steffen et al., 2014b).

Compressional stresses are applied due to ridge push east of Greenland at the Atlantic mid-ocean ridge towards the stable craton of North America to the west (Bird, 2003), which results in maximum east-west horizontal stress and minimum north-south horizontal stress. This stress direction for Greenland is confirmed by mantle flow models (Conrad & Behn, 2010), which indicate a horizontal mantle movement for the area offshore southern Greenland. In addition, a horizontal direction of the maximum stress is inferred in the World Stress Map offshore of the north-east of the United States (Heidbach et al., 2016), and studies of the palaeostress direction in the Palaeocene show a rotation of the maximum horizontal stresses from north-south to east-west going from the north-eastern coast (Peary Land) to the south-eastern coast (Skjoldungen; Guarnieri, 2015). Stresses in the north–south direction can be considered to be small and similar in magnitude to vertical stresses. This is due to lack of active plate boundaries to the south and north of Greenland (Bird, 2003), and is further supported by observations of palaeostresses along the eastern coast, which show a decrease of the intermediate stress magnitude from north to south (Guarnieri, 2015). Such a decrease in the intermediate stress magnitude relates to an increase of the stress ratio R from north to south (Guarnieri, 2015). This parameter links the maximum, medium and minimum stresses with each other (Etchecopar et al., 1981), and a high stress ratio of 0.95 is used here. The background stresses are calculated separately and not modelled as part of the GIA model, which implies that no plate boundaries need to be included into the GIA model.

2.1 Coulomb Failure Stress Changes

We use critically stressed conditions in the crust, which is valid for intraplate areas (Zoback & Townend, 2001), and analyse the change in Coulomb Failure Stress ΔCFS (Harris, 1998) which helps visualize stable and unstable seismic conditions. Put simply, positive values of this quantity represent unstable conditions indicating that seismic activity is likely, and negative values point to stable conditions where seismic activity is unlikely. Only two areas, the southern tip and northern coast of Greenland, experience unstable conditions in the early Holocene due to negative ice-mass changes (Fig. 2, Movie S1).

Figure 2

Seismic activity within deglaciating regions requires pre-existing faults, which can be reactivated to release the deglaciation-related stress build-up (Steffen et al., 2014b). Faults in North Greenland are mainly striking east–west (90°/180°) while those in south-western Greenland, close to the small town of Nanortalik, mainly strike northwest–southeast (135°/315°) and northeast–southwest (45°/225°; Guarnieri, 2015; Henriksen et al., 2009), although detailed regional fault parameters are lacking. ΔCFS calculations for various strike and dip values as well as stress ratios show that faults with strike values of 90° cannot be reactivated in the chosen stress setting (see Fig. S1 in the Supplementary Materials). Uenzelmann-Neben et al. (2012) identified a fracture zone offshore about 250 km to the south of Nanortalik, which shows disruptions of Pliocene sediment packages during the late Pleistocene. Peulvast et al. (2011) also identify possible small-scale deglacial glacially-triggered faults in the Sermilik area of south Greenland. We therefore focus on the south-western tip of Greenland, which becomes unstable at 10.615 ± 0.25 ka BP for our chosen model parameters (Fig. 2D). However, while glacially-triggered earthquakes in northern Europe have been identified using topographical changes and visible fault outcrops (Lagerbäck & Sundh, 2008), such large-scale features have not been observed in southern Greenland. Therefore, we look to observations of past relative sea-level (RSL) change to determine whether they are compatible with the timing and amplitude of faulting suggested by our model.

2.2 Relative sea level history in Nanortalik, Southern Greenland

Several RSL data sets have been collected in the area around Nanortalik (Fig. 3) with sea-level indicators from 13.511 ± 0.236 ka BP onwards (Bennike et al., 2002), thus covering the time when the area is predicted to have become unstable (Fig. 2D). These RSL data are of the highest quality – they are based on ^{14}C dated sediment samples from isolation basins which are rock depressions in the landscape that have been uplifted and isolated from the sea in the past (Bennike et al., 2002). The Nanortalik RSL data show rapid early Holocene sea-level fall from at least ~32 m above present around 13.8 ka cal BP to close to present by c. 10 ka cal BP, then falling to a lowstand in the early Holocene before rising to present in the late Holocene (Fig. 3C). Other Holocene RSL data in this region from Qaqortoq, 90 km NW of Nanortalik (Sparrenbom et al., 2006), and Igaliku, 100 km N of Nanortalik (Bierman et al., 2018) also show rapid early Holocene RSL fall.

We apply the deglaciation history of Huy3, which is based on a Greenland-wide ice extent and RSL database (Lecavalier et al., 2014), alongside the accompanying 1D Earth model within a GIA model to investigate the fit of the Huy3 GIA model to the Nanortalik RSL data. The majority of RSL data from around Greenland can be explained by Huy3 model reconstructions (Lecavalier et al., 2014). However, a misfit exists for data points in southern Greenland, and particularly at Nanortalik, especially for the four oldest data points. Extensive changes to the ice model history (Greenland and North America) and Earth model parameters have been unable to resolve the first-order misfit to these data points at Nanortalik (Fig. 3; Lecavalier et al., 2014). Even using a 3D Earth model in combination with the Huy3 ice model was not able to solve the misfit but decreased the difference between RSL points and modelled RSL in the early Holocene, and this 3D Earth model is also not able to fit the Nanortalik RSL data in the mid-to-late Holocene (Milne et al., 2018). Two additional ice model reconstructions were considered (ICE-5G (Peltier, 2004) and ANU (Fleming & Lambeck, 2004)) but the model fits were of lower quality than those for the Huy3 model (Fig. S2) and even larger discrepancies exist.

RSL predictions from Huy3 with the new 3D Earth model (Fig. 3C) indicate the deglacial marine limit was reached at c. 11 ka cal BP and rapid RSL fall occurred immediately thereafter (Fig. 3C). The ice history here is most likely inaccurate as suggested by Woodroffe et al. (2014) and Milne et al. (2018) because the timing of the marine limit being reached, which should correspond to initial deglaciation at the location, is ~3 ka too late given the evidence of ice-free conditions at lake N14 at 13.8 ka cal BP. Despite this issue with the timing of deglaciation, and therefore the timing of initial RSL fall in the Huy3 predictions, there still remains a significant discrepancy between the elevation of the RSL data before ~10.6 ka cal BP and the GIA model predictions. In particular lakes N14 and N18 are up to 14 m above the upper limit of uncertainty in the 3D Earth model (and 24 m above the lower uncertainty in this model) (Fig. 3C), and lakes N19 and N24, whilst falling within the upper limit of the 3D Earth model uncertainty, currently suggest a faster initial RSL fall compared to what might be predicted by an ice model with earlier deglaciation in this region (Woodroffe et al., 2014).

Figure 3

We therefore propose the hypothesis that tectonic activity may have led to the movement of the four RSL index points at Nanortalik older than ~10.6 ka. The occurrence of such an event would influence the elevation of RSL index points older than this age but not younger ones, thus bringing the RSL data into closer alignment with the Huy3 predictions (Figs. 3C, 4). As the sediments in the isolation basins N14, N18, N19 and N24 show no evidence for sea-level rise (i.e. a later transgression into the basin following initial isolation), this means a maximum correction of up to 16.5 m at any of the Nanortalik isolation basin locations (Fig. 3C, red boxes). Invoking a faulting event increases the fit between RSL curve predictions and faulting-corrected RSL heights (Fig. 4).

2.3 Fault Modelling

To simulate an earthquake due to the modelled stress changes, we created a two-dimensional (2D) GIA-fault model (Steffen et al., 2014b) and considered a range of plausible fault parameters (e.g. fault depth, fault width, friction). The stress and displacement results obtained from the 3D GIA model and stress analysis (described above) are used on a 2D profile together with the same Earth model parameters. The 2D profile is perpendicular to the strike direction (Fig. S3) and crosses the points N14, N18 and N19, but has a distance of about 15 km to N24. The element resolution is greatly increased compared to the 3D model and varies between 500 m in the crust to a few kilometers in the lower part of the lithosphere. We do not apply the Huy3 ice model but use the corresponding stresses for each time step of the 3D GIA model and implement them in the 2D GIA-fault model. As discussed above, the tectonic regime in southern Greenland indicates that deglaciation would most likely result in thrust faulting with a strike orientation that is NW-SE (or SE-NW). Of all the faults we considered, via a set of parameter values for dip, strike and friction (see Fig. S1), the one described below is the most likely to have been reactivated based on the offsets indicated by the RSL data. The modelled offshore thrust fault southwest of Nanortalik (Fig. 4A) results in a surface deformation that uplifts all RSL data points older than 10.6 ka in the area of Nanortalik. This fault has a dip of 45° and extends from a depth of 5 km to 24 km and hence does not outcrop at the surface; its strike is parallel to the outer coast at 315° and is thus parallel to surface faults identified in this area.

An additional parameter in the modelling of the fault displacement is the coefficient of friction. Steady-state and static friction values are defined along the fault surface. Observations show that the steady-state friction is about 10 – 30% of the static friction (Di Toro et al., 2011). The steady-state μ_{ss} and static friction μ_k are related to each other in ABAQUS (Hibbitt et al., 2016):

$$\mu = \mu_{ss} + (\mu_k - \mu_{ss}) * e^{-d_c} .$$

The decay coefficient d_c is assumed to be 1.0, as this would equal the equation presented in Di Toro et al. (2011) for laboratory earthquakes Here, we use a static friction of 0.6 and a steady-state friction of 0.12 (20% of the static friction). As the friction is unknown, we calculate an uncertainty due to this by applying steady-state frictions of 0.06 and 0.18 as well due to the observed changes between 10% and 30% (Di Toro et al., 2011), respectively. The duration of the earthquake is chosen to be 10 seconds as the average rupture velocity is between 2.6 and 3.0 km/s (Heaton, 1990), which results in a duration of 10.4 to 9 s for this specific fault with a width of ~27 km. However, in the estimation of the uncertainty (Fig. 4A) we also consider different durations (1 s to 60 s) of the rupture propagation. Nevertheless, a specific post-seismic phase was not included. The displacement of such an additional phase is also mostly smaller than the co-seismic phase. The stress release of the earthquake is applied to the GIA and background stresses in the subsequent time steps and no further instability occurs until today at this location. We note that our calculations neglect the influence of pore-fluid pressure as no information is available on how this parameter changes in a crustal setting beneath the ice and at the ice margin during a glacial cycle.

In our model, the fault is reactivated at 10.615±0.25 ka BP with a fault slip of 43.7 m (Fig. S3), equivalent to an earthquake with a moment magnitude of about 8.3 using a fault length of 200 km. The displacement at the surface is 38.1 m (Fig. 4), which would normally relate to a calculated surface rupture length of at least 800 km using standard calculation methods (Wells & Coppersmith, 1994). However, Mattila et al. (2018) showed that GIFs appear to have a higher displacement-length ratio than the standard calculation would allow, and are usually shorter than 200 km. We therefore apply a fault length of 200 km for our Greenland faulting event based on the maximum length of GIFs found in northern Europe. This creates a moment magnitude which is larger compared to estimates for other GIFs, but those previous estimates are based on fault offsets visible at the surface and slip within the crust was most likely larger in this instance due to the increase in displacement towards the fault centre (e.g., Kobayashi et al., 2015). In addition, the ratio of average subsurface displacement to average surface displacement is mostly larger than 1 (Wells & Coppersmith, 1994) indicating a larger subsurface displacement than what is seen at the Earth's surface.

Earthquakes with such a large magnitude are rare and usually occur along active, convergent, plate boundaries rather than the intraplate setting considered here. If we consider the occurrence of several earthquakes instead of one single event, the magnitude could be decreased. Recent results by Smith et al. (2018) also showed that offsets along GIFs in northern Sweden were not created in one event but rather two or more events. The total fault slip of 47.3 m could be divided into ten events with 4.73 m slip each. This decrease in the fault slip would mean smaller surface displacements, which would allow the rupture length to be reduced to 100 km (Wells & Coppersmith, 1994). This change in the fault length and fault slip results in a decrease of the moment magnitude to 5.8 for each of the ten earthquakes, which is also more commonly observed for intraplate earthquakes (e.g., Mooney et al., 2012). However, the RSL data as well as geological maps allow no differentiation between one-large magnitude 8.3 event vs a series of smaller events over decades to centuries with lower magnitudes. Thus, neither only one nor several earthquakes can be excluded, and further field observations are necessary (e.g., fault mapping, fault dating) to identify and constrain the occurrence of any seismic activity in this area during the early Holocene. Even though the strike direction of the fault (315°) is like that of faults observed in the Nanortalik region, this specific fault has not been identified, which may be due to the location of the fault being offshore and the lack of high-quality, high-resolution seismic data in this region (Uenzelmann-Neben et al., 2012).

Figure 4

The vertical displacement at the surface induced by this modelled earthquake would increase the elevation of RSL observations older than 10.6 ka by 10.8 to 19.0 m (Fig. 4A).

These displacements move the observations to within the Huy3 3D Earth model uncertainty range (Fig. 4B). One data point, N24, is too low using the vertical displacement correction, indicating that the fault movement is excessive (Fig. 4B). This includes the parametric uncertainties associated with the 2D fault model as well as the unmodelled slip dependency along the fault in the strike direction. Fault slip models of previous large earthquakes show strong lateral variations along strike (e.g., Kobayashi et al., 2015), which have not been modelled here. A change in the vertical displacement based on a smaller fault slip magnitude could decrease the fault offset by up to 25% over a distance of only 10 to 15 km. The location of the RSL index point N24 is 15 km along strike relative to the other RSL data. This could lead to a decrease of the fault offset from 19.0 m to 14.25 m, moving the N24 index point up to within the vertical error of stratigraphic position and within the range of possible GIA model runs (Fig. 4B). In addition, local variations in the geology and potentially a system of faults rather than just one fault could lead to slightly different fault displacements and enhance (or reduce) the quality of fit. However, this cannot be solved using the homogeneous Earth models applied here and so is a target for future research.

Although geomorphological evidence for a reactivation event c. 10,600 years ago has not been found offshore south Greenland, the misfit between the RSL observations and predictions and the timing of unstable conditions does suggest that there may have been tectonic activity at this time. Importantly seismic data offshore south Greenland has not been analysed with this event in mind. In northern Europe GIFs have been mainly identified by visible offsets at the surface, but in recent years soft sediment structures and high-resolution elevation data have revealed new, previously undetected GIFs (Berglund & Dahlström, 2015; Smith et al., 2018). Elevation changes due to an earthquake offshore south Greenland may also be difficult to spot as the bathymetric data for this area have a poor resolution and a gradient of less than 4.5 m/km both onshore and offshore would be obtained from the vertical fault displacement at the surface (Fig. 4A), which is difficult to identify in the landscape. As RSL data are crucial constraints for ice model calibrations we suggest that RSL data proximal to ice sheets should be investigated for vertical displacement caused by faulting due to ice retreat, otherwise glaciological simulations might be biased in certain regions, e.g., Greenland, the Canadian Arctic and the Barents Sea.

The southern tip of Greenland is an area of high seismicity compared to other parts of Greenland today (Voss et al., 2016), but recent earthquake magnitudes are mostly below 3.0 (Fig. S4), which is similar to the ones observed today at one of the GIFs in Fennoscandia (Pärvie fault; Lindblom et al., 2015). In addition, Voss et al. (2016) noted that many more earthquakes can be identified if the seismic station density were increased (currently only two stations, Fig. S4) and the magnitude of completeness could be decreased to below 3. A large uncertainty exists also on the location of the events and is mostly above 100 km for earthquakes recorded by these two stations (Voss et al., 2016). Therefore, previous moderate to large magnitude seismicity at the location of the hypothesised reactivated fault is a possibility.

2.4 Tsunami generation

Vertical displacement of the sea floor can produce tsunami waves. We use the slip distribution of the 2D model, the modern-day bathymetry of the Atlantic Ocean and that stress was released in the worst-case scenario of a single event to evaluate if a significant tsunami could have been created by the modelled earthquake with a slip of 47.3 m. The obtained 2D fault slip is interpolated to a 3D distribution towards the edges of the fault (Fig. 5A) and the regional mean sea-level has been decreased by 35.2 m, which is the eustatic sea-level of Huy3 at 10.615 ka. We use GeoClaw to simulate the dynamics of the generated tsunamis. GeoClaw is part of ClawPack (George, 2008) and solves the depth-averaged Shallow Water Equation using a finite volume method on adaptively refining grids (Mandli & Nawson, 2014). GeoClaw has been validated and verified using the standard benchmarks as defined by NOAA (National Oceanic and Atmospheric Administration; Synolakis, 1991) and has been applied to a variety of tsunami-related problems (Berger et al., 2011; Arcos & LeVeque, 2015). We do not consider tides in our simulations.

Based on the simulated earthquake characteristics, our results for the worst-case scenario (moment magnitude of 8.3 for a fault length of 200 km) suggest a sizable tsunami that would have impacted the shorelines of North America and Europe (Fig. 5B). Greenland would have experienced the largest tsunami waves (generally exceeding 1.5 m with a maximum of 7.2 m at the southern tip). Tsunami waves up to 1.5 m in amplitude would also have reached North America (Fig. 5B), while those reaching Europe have maximum tsunami elevations between 0.5 and 1 m (Fig. 5B). Note that these maxima are retrieved from the simulations in 50-m water depth and the tsunami wave elevation increases as they approach the shore. This process is known as shoaling and causes the tsunami-wave amplitude to grow by a factor between 4 and 6 (Synolakis, 1991), resulting in a maximum runup of about 7.5 m and 5 m along North American and European coasts, respectively. Smaller tsunami waves would be created when using the other scenario with ten separate events with fault slips of 4.73 m each along a 100 km fault (see Fig. S5). One event would have produced run-up wave heights of up to 0.5 m along the southern Greenland coast but only a few decimetres along the Canadian and European coasts (Fig. S5).

Figure 5

Tsunami deposits related to the offshore Nanortalik earthquake have not been identified, but there may be several potential reasons for this. Although the far southwest Greenland coast was ice free by this time, the interaction of any tsunami waves with permanent or seasonal sea ice in coastal areas would have decreased the tsunami impact significantly. Across Baffin Bay the Labrador coast had grounded ice extending to the present-day shoreline (Tarasov et al., 2012; Vacchi et al., 2018), as did the coast of Iceland (Peltier, 2004). Along the western Newfoundland coast, and in many other ice-free areas of the North Atlantic, RSL was metres to tens of metres below present at the time (Fig. 5C). Thus, any tsunami deposits would now lie offshore, and it is extremely unlikely that sedimentary evidence will have been preserved through the subsequent marine transgression to present (Vacchi et al., 2018). Therefore, even if a single-event earthquake and tsunami did occur it might not be possible to find related tsunami deposits. Nevertheless, given that the predicted fault occurred offshore, the theoretical potential for tsunami generation is high and thus offers an additional avenue to test our hypothesis in the future.

3. CONCLUSION

The release of glacially-induced stresses leads to the creation of earthquakes as has been recorded in parts of northern Europe from geological evidence. We propose the occurrence of glacially-induced faulting offshore Nanortalik (south-western tip of Greenland) in the early Holocene based on stress modelling and the discrepancy between GIA model predictions and RSL data from this region. The stress release could have been associated with a single, 8.2 magnitude event or a series of moderate to strong magnitude earthquakes. If the stress release was dominated by a single event, it may have generated a tsunami (Fig. 1); with preliminary model simulations indicating that run-up heights of several metres would be possible along eastern and western North Atlantic coasts. As ice-sheet melting on Greenland is ongoing, other areas could become unstable in the future providing a potential future danger for countries bordering the North Atlantic, if offshore faults were to be reactivated again.

ACKNOWLEDGEMENTS

We thank Kristian K. Kjeldsen (Geological Survey of Denmark and Greenland) for providing geological maps and Ken McCaffrey (Durham University) for discussions.

REFERENCES

M.E.M. Arcos, R.J. LeVeque, Validating Velocities in the GeoClaw Tsunami Model Using Observations near Hawaii from the 2011 Tohoku Tsunami. *Pure and Applied Geophysics* **172**, 849-867 (2015). doi:10.1007/s00024-014-0980-y

R. Arvidsson, Fennoscandian Earthquakes: Whole Crustal Rupturing Related to Postglacial Rebound. *Science* **274**, 744-746 (1996). doi:10.1126/science.274.5288.744

O. Bennike, S. Björck, K. Lambeck, Estimates of South Greenland late-glacial ice limits from a new relative sea level curve. *Earth and Planetary Science Letters* **197**, 171–186 (2002). doi:10.1016/S0012-821X(02)00478-8

M.J. Berger, D.L. George, R.J. LeVeque, K.T. Mandli, The GeoClaw software for depth-averaged flows with adaptive refinement. *Advances in Water Resources* **34**, 1195-1206 (2011). doi:10.1016/j.advwatres.2011.02.016

M. Berglund, N. Dahlström, Post-glacial fault scarps in Jämtland, central Sweden. *GFF* **137**(4), 339–343 (2015). doi:10.1080/11035897.2015.1036361

P.R. Bierman, J. Shakun, E. Portenga, D. Rood, L.B. Corbett, Directly dating post-glacial Greenlandic emergence at high resolution using in situ 10Be. *Quaternary Research* **90**, 110-126 (2018). doi:10.1017/qua.2018.6

P. Bird, An updated digital model of plate boundaries. *Geochemistry, Geophysics, Geosystems* **4**, 1027 (2003). doi:10.1029/2001GC000252

C. Brandes, T. Plenefisch, D.C. Tanner, N. Gestermann, H. Steffen, Evaluation of deep crustal earthquakes in northern Germany – Possible tectonic causes. *Terra Nova* **31**, 83-93 (2019). doi:10.1111/ter.12372

C.P. Conrad, M.D. Behn, Constraints on lithosphere net rotation and asthenospheric viscosity from global mantle flow models and seismic anisotropy. *Geochemistry, Geophysics, Geosystems* **11**, Q05W05 (2010). doi:10.1029/2009GC002970

G. Di Toro, R. Han, T. Hirose, N. De Paola, S. Nielsen, K. Mizoguchi, F. Ferri, M. Cocco, T. Shimamoto, Fault lubrication during earthquakes, *Nature* **471**, 494-498 (2011). doi:10.1038/nature09838

A. Etchecopar, G. Vasseur, M. Daignieres, An inverse problem in microtectonies for the determination of stress tensors from fault striation analysis. *Journal of Structural Geology* **3**(1), 51-65 (1981). doi:10.1016/0191-8141(81)90056-0

K. Fleming, K. Lambeck, Constraints on the Greenland Ice Sheet since the Last Glacial Maximum from sea-level observations and glacial-rebound models. *Quaternary Science Reviews* **23**, 1053–1077 (2004). doi:10.1016/j.quascirev.2003.11.001

D.L. George, Augmented Riemann Solvers for the Shallow Water Equations over Variable Topography with Steady States and Inundation. *Journal of Computational Physics* **227**, 3089-3113 (2008). doi:10.1016/j.jcp.2007.10.027

J.W. Gephart, D.W. Forsyth, An improved method for determining the regional stress tensor using earthquake focal mechanism data: Application to the San Fernando Earthquake Sequence. *Journal of Geophysical Research* **89**, 9305–9320 (1984). doi:10.1029/JB089iB11p09305

P. Guarnieri, Pre-break-up palaeostress state along the East Greenland margin. *Journal of the Geological Society* **172**, 727-739 (2015). doi:10.1144/jgs2015-053

R.A. Harris, Introduction to Special Section: Stress Triggers, Stress Shadows, and Implications for Seismic Hazard. *Journal of Geophysical Research* **103**, 24347-24358 (1998). doi:10.1029/98JB01576

T.H. Heaton, Evidence for and implications of self-healing pulses of slip in earthquake rupture. *Physics of the Earth and Planetary Interiors* **64**, 1 – 20 (1990). doi:10.1016/0031-9201(90)90002-F

O. Heidbach, M. Rajabi, X. Cui, K. Fuchs, B. Müller, J. Reinecker, K. Reiter, M. Tingay, F. Wenzel, F. Xie, M.O. Ziegler, M.-L. Zoback, M. Zoback, The World Stress Map database release 2016: Crustal stress pattern across scales. *Tectonophysics* **744**, 484-498 (2018). doi:10.1016/j.tecto.2018.07.007

N. Henriksen, A.K. Higgins, F. Kalsbeek, T.C.R. Pulvertaft, Greenland from Archean to Quaternary. *Geological Survey of Denmark and Greenland Bulletin Bulletin* **18**, 126 p. (2009).

D. Hibbitt, B. Karlsson, P. Sorensen, Getting Started with ABAQUS – Version 2016. Hibbitt, Karlsson & Sorensen, Inc. (2016).

A.C. Johnston, Suppression of earthquakes by large continental ice sheets. *Nature* **330**, 467-469 (1987). doi:10.1038/330467a0

K. Katsumata, M. Kosuga, H. Katao, T. Yamada, A. Kato, Research Group for the Joint Seismic Observations at the Nobi Area, Focal mechanisms and stress field in the Nobi fault area, central Japan. *Earth, Planets and Space* **67**, 99 (2015). doi:10.1186/s40623-015-0275-2

G. Kaufmann, P. Wu, E.R. Ivins, Lateral viscosity variations beneath Antarctica and their implications on regional rebound motions and seismotectonics, *Journal of Geodynamics* **39**, 165-181 (2005). doi:10.1016/j.jog.2004.08.009.

S.A. Khan, I. Sasgen, M. Bevis, T. van Dam, J.L. Bamber, J. Wahr, M. Willis, K.H. Kjær, B. Wouters, V. Helm, B. Csatho, K. Fleming, A.A. Bjørk, A. Aschwanden, P. Knudsen, P. Kuipers Munneke, Geodetic measurements reveal similarities between post–Last Glacial Maximum and present-day mass loss from the Greenland ice sheet. *Science Advances* **2**, e1600931 (2016). doi:10.1126/sciadv.1600931

T. Kobayashi, Y. Morishita, H. Yarai, Detailed crustal deformation and fault rupture of the 2015 Gorkha earthquake, Nepal, revealed from ScanSAR-based interferograms of ALOS-2. *Earth, Planets and Space* **67**, 201 (2015). doi:10.1186/s40623-015-0359-z

R. Lagerbäck, M. Sundh, Early Holocene faulting and paleoseismicity in Northern Sweden. *Sveriges geologiska undersökning*, Research paper C **836**, 84 p. (2008).

B.S. Lecavalier, G.A. Milne, M.J.R. Simpson, L. Wake, P. Huybrechts, L. Tarasov, K.K. Kjeldsen, S. Funder, A.J. Long, S. Woodroffe, A.S. Dyke, N.K. Larsen, A model of Greenland ice sheet deglaciation constrained by observations of relative sea level and ice extent. *Quaternary Science Reviews* **102**, 54-84 (2014). doi:10.1016/j.quascirev.2014.07.018

E. Lindblom, B. Lund, A. Tryggvason, M. Uski, R. Bödvarssson, C. Juhlin, R. Roberts, Microearthquakes illuminate the deep structure of the endglacial Pärvie fault, northern Sweden. *Geophysical Journal International* **201**, 1704-1716 (2015). doi:10.1093/gji/ggv112

K.T. Mandli, C.N. Dawson, Adaptive mesh refinement for storm surge. *Ocean Modelling* **75**, 36-50 (2014). doi:10.1016/j.ocemod.2014.01.002

J. Mattila, A. Ojala, T. Ruskeeniemi, J.-P. Palmu, M. Markovaara-Koivisto, N. Nordbäck, R. Sutinen, On the displacement-length ratios of postglacial faults. Extended abstract in “Kukkonen, I., et al. (Eds.), Lithosphere 2018 – Tenth Symposium on the Structure, Composition and Evolution of the Lithosphere. Programme and Extended Abstracts, Oulu, Finland, November 14-16, 2018”, 77-80 (2018).

M. McMillan, A. Leeson, A. Shepherd, K. Briggs, T.W.K. Armitage, A. Hogg, P. Kuipers Munneke, M. van den Broeke, B. Noël, W.J. van de Berg, S. Ligtenberg, M. Horwath, A. Groh, A. Muir, L. Gilbert, A high-resolution record of Greenland mass balance. *Geophysical Research Letters* **43**, 7002–7010 (2016). doi:10.1002/2016GL069666

G.A. Milne, K. Latychev, A. Schaeffer, J.W. Crowley, B.S. Lecavalier, A. Audette, The influence of lateral Earth structure on glacial isostatic adjustment in Greenland. *Geophysical Journal International* **214**, 1252-1266 (2018). doi:10.1093/gji/ggy189

J.X. Mitrovica, J.L. Davis, I.I. Shapiro, A spectral formalism for computing three–dimensional deformations due to surface loads 1. Theory. *J. geophys. Res.* **99**(B4), 7057–7073 (1994). doi: 10.1029/93JB03128.

W.D. Mooney, J. Ritsema, Y.K. Hwang, Crustal seismicity and the earthquake catalog maximum moment magnitude (M_{cmax}) in stable continental regions (SCRs): Correlation with the seismic velocity of the lithosphere. *Earth and Planetary Science Letters* **357-358**, 78-83 (2012). doi:10.1016/j.epsl.2012.08.032

M. Olivieri, G. Spada, Ice melting and earthquake suppression in Greenland. *Polar Science* **9**, 94-106 (2015). doi:10.1016/j.polar.2014.09.004

W.R. Peltier, Global glacial isostasy and the surface of the ice-age Earth: The ICE-5G (VM2) model and GRACE. *Annual Review of Earth and Planetary Sciences* **32**, 111-149 (2004). doi:10.1146/annurev.earth.32.082503.144359

J-P. Peulvast, J.A. Bonow, P. Japsen, R.W. Wilson, K.J.W. McCaffrey, Morphostructural patterns and landform generations in a glaciated passive margin: the Kobberminebugt-Qaqortoq region of South Greenland. *Geodynamica Acta* **24**, 1-19 (2011).

C.A. Smith, S. Grigull, H. Mikko, Geomorphic evidence of multiple surface ruptures of the Merasjärvi "postglacial fault", northern Sweden. *GFF* **140**, 318-322 (2018). doi:10.1080/11035897.2018.1492963

C.J. Sparrenbom, O. Bennike, S. Björck, K. Lambeck, Holocene relative sea-level changes in the Qaqortoq area, southern Greenland. *Boreas* **35**, 171-187 (2006). doi:10.1080/03009480600578032

R. Steffen, P. Wu, H. Steffen, D.W. Eaton, The effect of earth rheology and ice-sheet size on fault slip and magnitude of postglacial earthquakes. *Earth and Planetary Science Letters* **388**, 71-80 (2014a). doi:10.1016/j.epsl.2013.11.058

R. Steffen, P. Wu, H. Steffen, D.W. Eaton, On the implementation of faults in finite-element glacial isostatic adjustment models. *Computers & Geosciences* **62**, 150-159 (2014b). doi:10.1016/j.cageo.2013.06.012

R. Steffen, H. Steffen, P. Wu, D.W. Eaton, Reply to comment by Hampel et al. on "Stress and fault parameters affecting fault slip magnitude and activation time during a glacial cycle". *Tectonics* **34** (2015). doi:10.1002/2015TC003992

H. Steffen, R. Steffen, L. Tarasov, Modelling of glacially-induced stress changes in Latvia, Lithuania and the Kaliningrad District of Russia. *Baltica* **32**, 78-90 (2019). doi: 10.5200/baltica.2019.1.7

C.E. Synolakis, Green's law and the evolution of solitary waves. *Physics of Fluids A: Fluid Dynamics* **3**, 490 (1991). doi:10.1063/1.858107

L. Tarasov, A.S. Dyke, R.M. Neal, W.R. Peltier, A data-calibrated distribution of deglacial chronologies for the North American ice complex from glaciological modelling. *Earth and Planetary Science Letters* **315–316**, 30–40 (2012). doi:10.1016/j.epsl.2011.09.010

G. Uenzelmann-Neben, D.N. Schmidt, F. Niessen, R. Stein, Intraplate volcanism off South Greenland: caused by glacial rebound? *Geophysical Journal International* **190**, 1–7 (2012). doi:10.1111/j.1365-246X.2012.05468.x

M. Vacchi, S.E. Engelhart, D. Nikitina, E.L. Ashe, W.R. Peltier, K. Roy, R.E. Kopp, B.P. Horton, Postglacial relative sea-level histories along the eastern Canadian coastline. *Quaternary Science Reviews* **201**, 124-146 (2018). doi:10.1016/j.quascirev.2018.09.043

P. Voss, S. Kildegaard Poulsen, S. Simonsen, S. Gregersen, Seismic hazard assessment of Greenland. *Geological Survey of Denmark and Greenland Bulletin Bulletin* **13**, 57–60 (2007).

P.H. Voss, T.B. Larsen, T. Dahl-Jensen, Earthquakes in Greenland – a review. Abstract ESC2016-220 presented at the 35th General Assembly of the European Seismological Commission, Trieste, Italy, 4-10 September (2016).

D.L. Wells, K.J. Coppersmith, New Empirical Relationships among Magnitude, Rupture Length, Rupture Width, Rupture Area, and Surface Displacement. *Bulletin of the Seismological Society of America* **84**(4), 974-1002 (1994).

P. Wu, Using commercial finite element packages for the study of earth deformations, sea levels and the state of stress. *Geophysical Journal International* **158**, 401-408 (2004). doi:10.1111/j.1365-246X.2004.02338.x

P. Wu, W.R. Peltier, Viscous gravitational relaxation. *Geophysical Journal of the Royal Astronomical Society* **70**, 435-485 (1982). doi:10.1111/j.1365-246X.1982.tb04976.x

P. Wu, H.S. Hasegawa, Induced stresses and fault potential in eastern Canada due to a disc load: a preliminary analysis. *Geophysical Journal International* **127**, 215–229 (1996). doi: 10.1111/j.1365-246X.1996.tb01546.x

M.D. Zoback, J. Townend, Implications of hydrostatic pore pressures and high crustal strength for the deformation of intraplate lithosphere. *Tectonophysics* **336**, 19-30 (2001). doi:10.1016/S0040-1951(01)00091-9

FIGURES

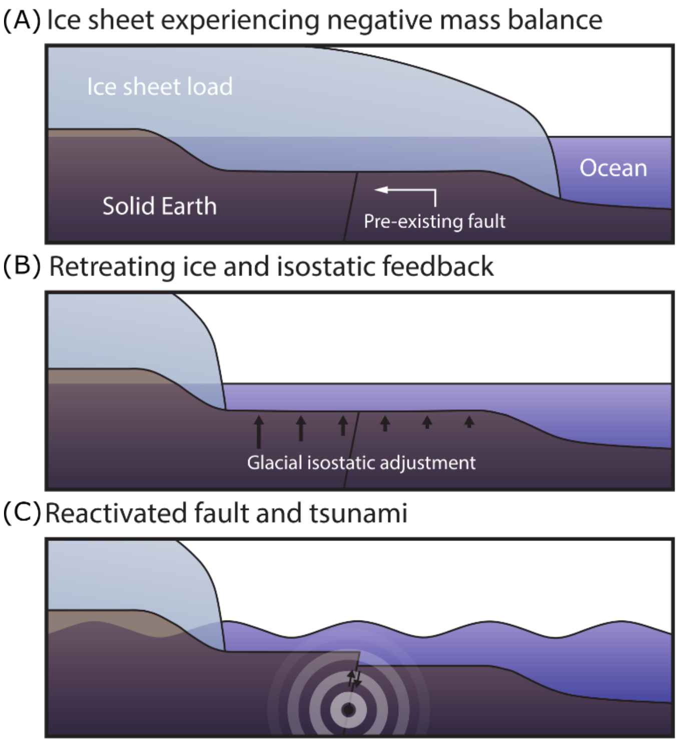

Fig. 1: Stages of glacially-induced fault reactivation and tsunami development. (A) The ice sheet undergoes negative mass balance in response to climate warming. (B) Ice sheet retreat causes a viscoelastic glacial isostatic response from the solid Earth. (C) Due to an asynchronous decrease of horizontal and vertical stresses in a compressional stress setting, a pre-existing fault is reactivated triggering an earthquake and tsunami.

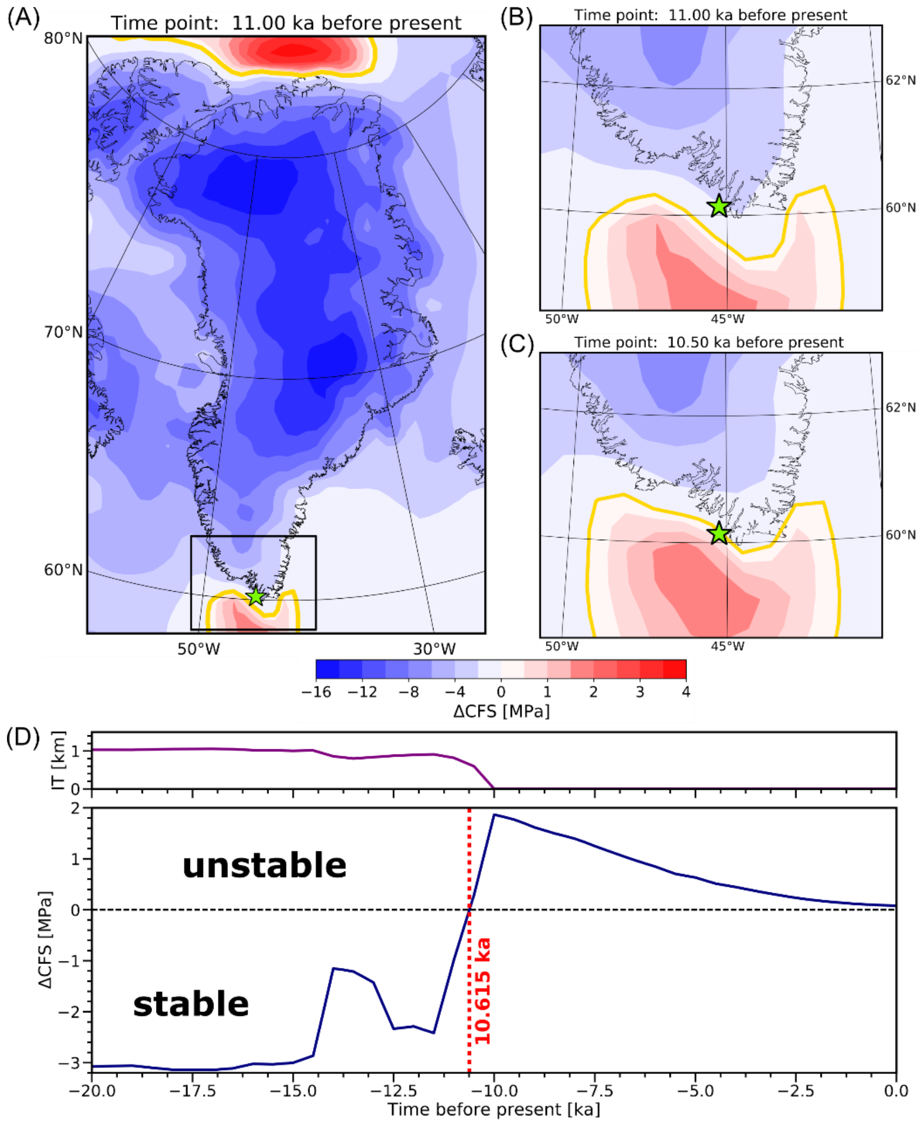

Fig. 2: Stress variations for Greenland in the Holocene. The ΔCFS (Change in Coulomb Failure Stress) is shown at 11 ka BP (A) for entire Greenland, and at 11 ka BP (B) and 10.5 ka BP (C) for southern Greenland. The area in (B) and (C) is marked by a black square in (A). The yellow line marks the change from stable (blue) to unstable (red) conditions. (D) The ΔCFS over time for the last 20 ka for southern Greenland (green star in (A), (B) & (C)). A potential fault with a dip of 45°, a strike of 315° and a coefficient of internal friction of 0.6 is assumed. The area becomes unstable at 10.615 ka BP (marked by red-dashed line). The ice thickness (IT) variation is shown on top as a purple line.

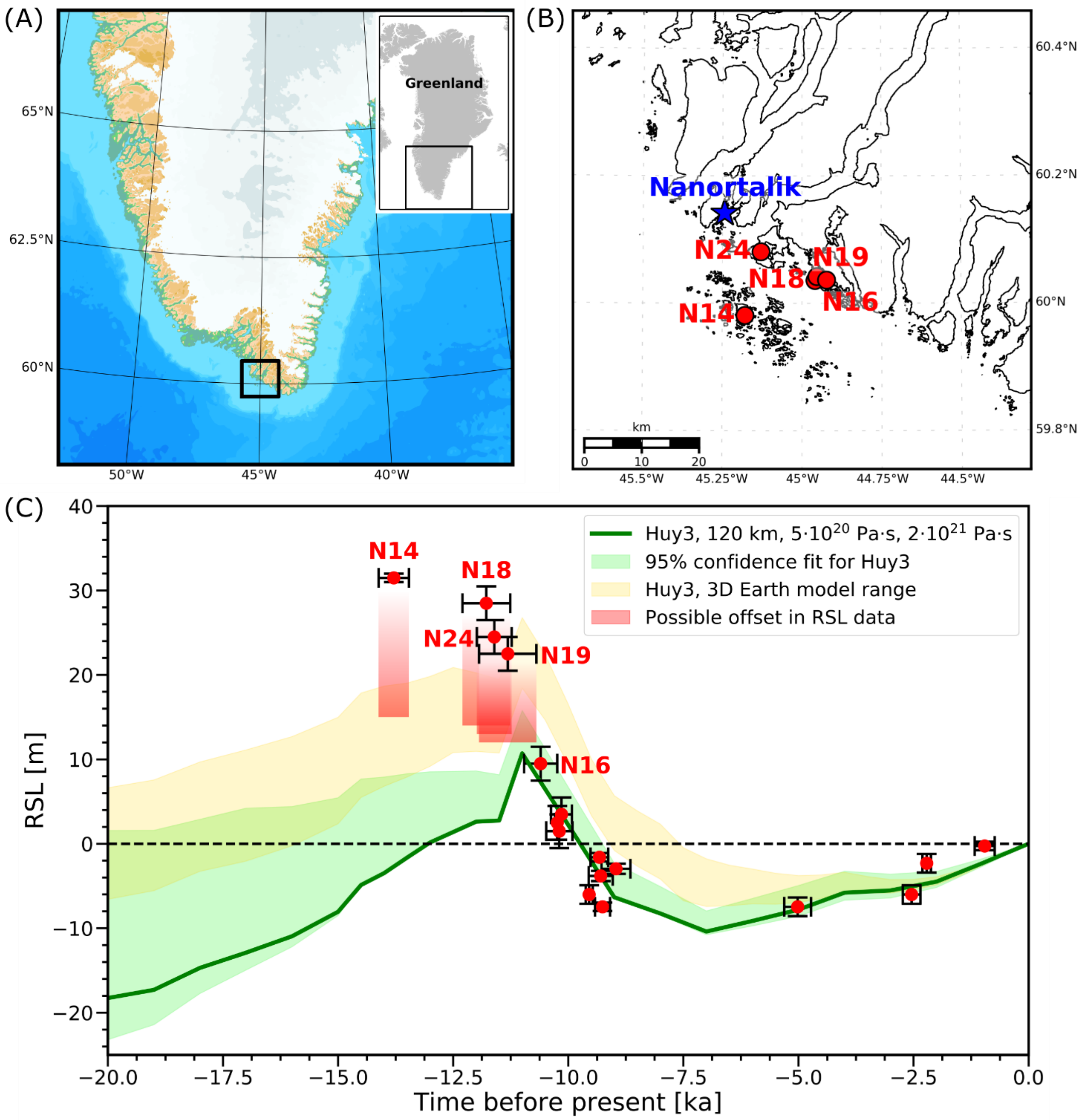

Fig. 3: Geography of southern Greenland and relative-sea level observations at Nanortalik. (A) Geographical overview of southern Greenland. Black rectangle shows area in (B). (B) Location of RSL observations and the town of Nanortalik. (C) RSL observations and predictions using Huy3. The green line is obtained from the best-fitting Earth model with a lighter green bounding envelop based on RSL curves using the nominal 95% confidence interval Earth models (described in Table 2 of Lecavalier et al. (2014)). A range of RSL curve predictions using various 3D Earth models (yellow area) indicate the range of further RSL curves (after Milne et

al., 2018). The RSL observations are shown with 2-σ uncertainty in the time and height range as black bars. The maximum possible offset to allow a better to fit to the RSL predictions as well as to have an RSL fall only are shown as red squares for N14, N18, N19 and N24.

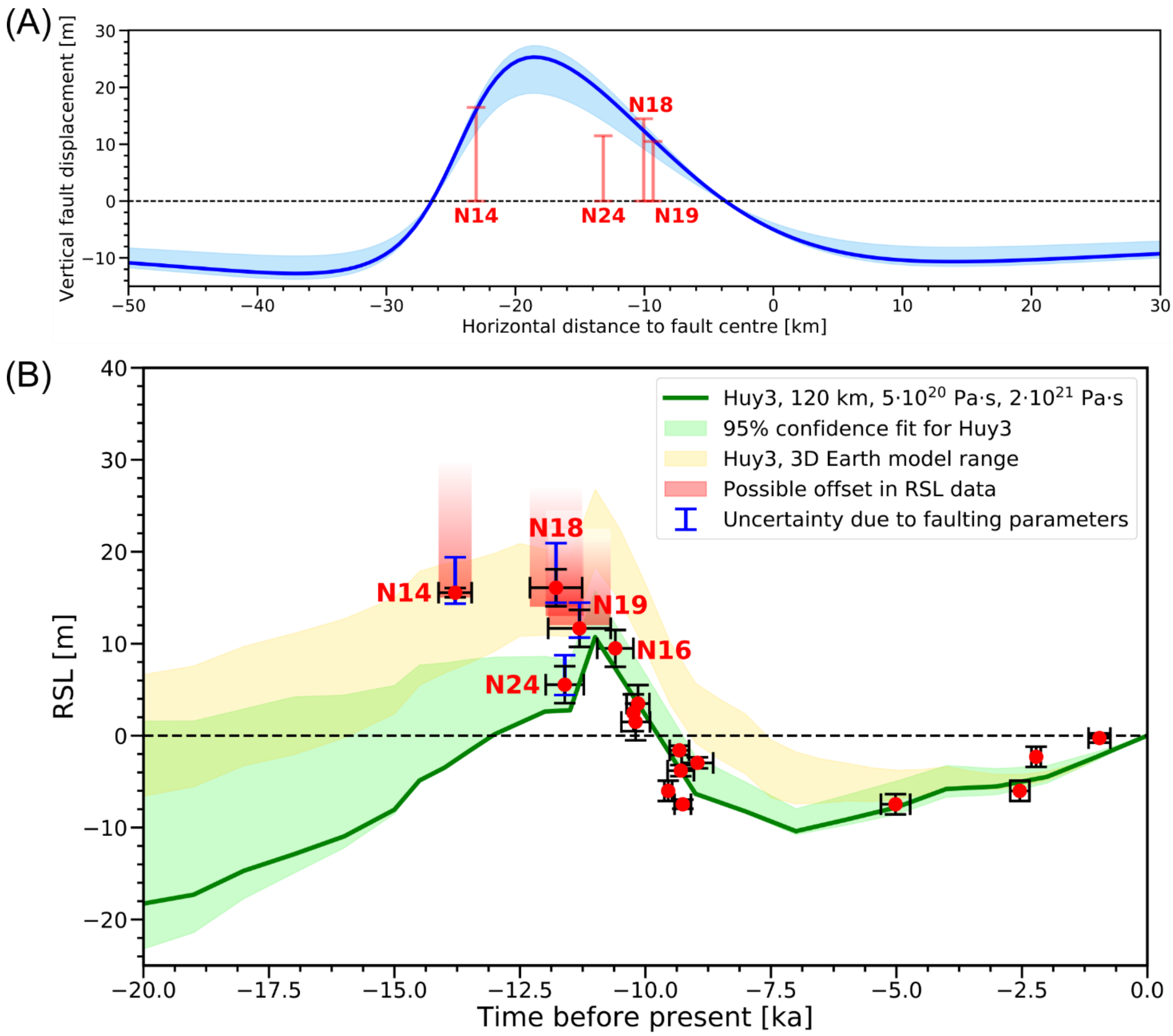

Fig. 4: Vertical fault displacement and estimated corrections for the RSL points. The vertical fault displacement is obtained for a fault dipping at 45° and extending between 5 and 24 km depth. Results are based on values of 0.6 and 0.12 for static and steady-state friction, respectively. (A) Vertical displacement vs. horizontal distance to fault centre projected on the model Earth surface with parametric uncertainty (light-blue) associated with using a steady-state coefficient of friction between 0.06 and 0.18 and different rupture times. RSL heights with maximum possible offset are shown in red. (B) Modified RSL data points for Nanortalik considering the correction of the RSL observations by the obtained vertical fault displacement. The blue bars mark the uncertainty associated with parametric uncertainty from the fault modelling (light-blue area shown in (A)).

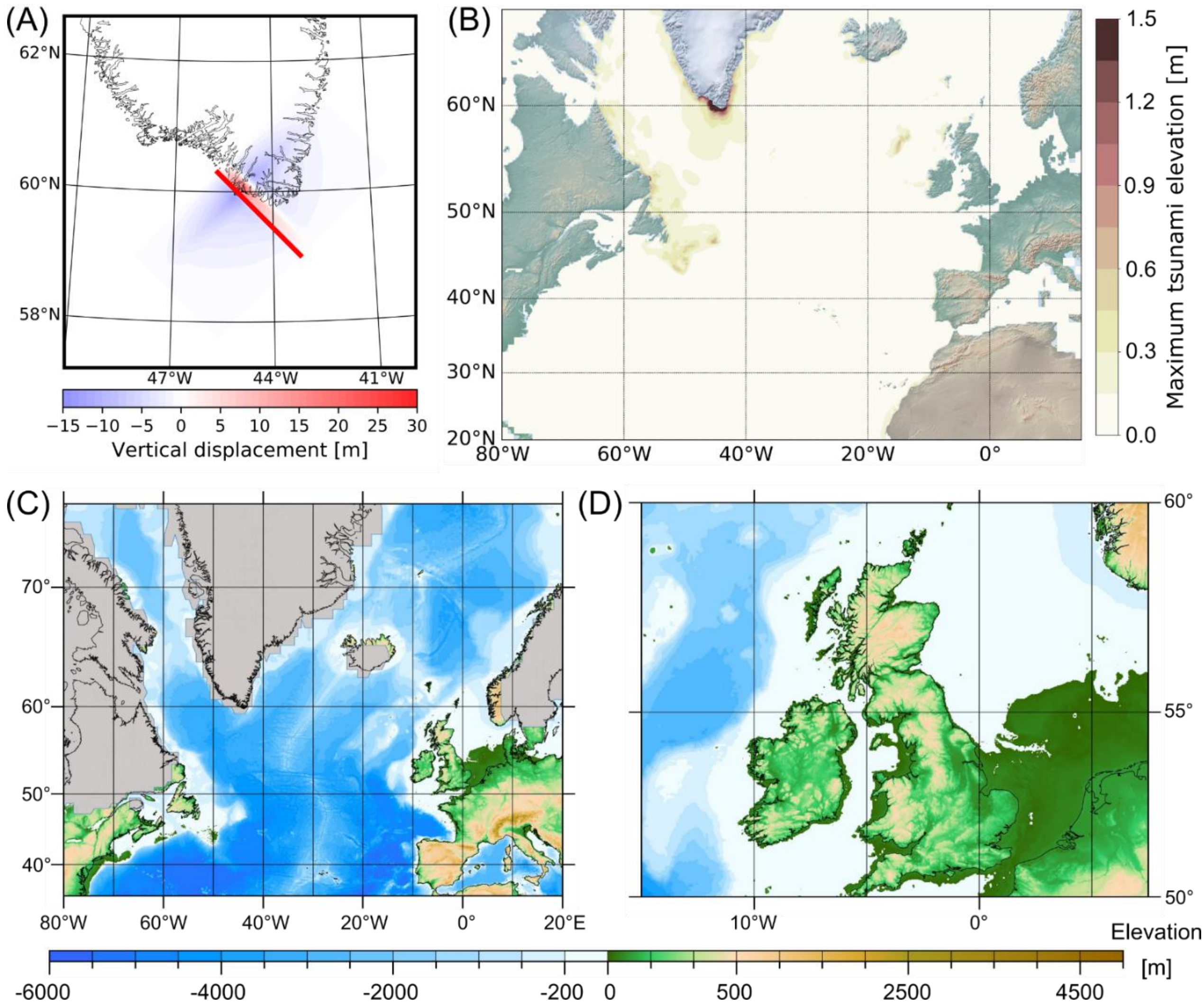

Fig. 5: Fault displacement and their corresponding tsunami deep-water wave amplitude as well as paleogeographic overview of the North Atlantic region. (A) Vertical fault displacement interpolated to the edges of the fault trace for a fault length of 200 km. (B) The distribution of the deep-water wave amplitude over the entire North Atlantic using a single earthquake with a fault slip of 47.3 m. (C) Modelled paleogeography (using the optimal 1-D model from Lecavalier et al. (2014) together with Huy3) and Huy3 (Lecavalier et al., 2014) ice-sheet distribution (grey) of the North Atlantic region at 10.6 ka BP. (D) Same as (C) but for the western European coast.